J. Fluid Mech. (2009), *vol.* 622, *pp.* 291–320. © 2009 Cambridge University Press
doi:10.1017/S0022112008005338 Printed in the United Kingdom

Pulsatile flow in stenotic geometries: flow behaviour and stability

M. D. GRIFFITH[1,2]†, T. LEWEKE[2], M. C. THOMPSON[1]
AND K. HOURIGAN[1]

[1]Fluids Laboratory for Aeronautical and Industrial Research (FLAIR), Department of Mechanical
and Aerospace Engineering & Division of Biological Engineering, Monash University,
Melbourne, Victoria 3800, Australia

[2]Institut de Recherche sur les Phénomènes Hors Equilibre (IRPHE), CNRS/Universités Aix-Marseille,
49 rue Frédéric Joliot-Curie, BP 146, F-13384 Marseille Cedex 13, France

(Received 3 April 2008 and in revised form 26 November 2008)

Pulsatile inlet flow through a circular tube with an axisymmetric blockage of varying size is studied both numerically and experimentally. The geometry consists of a long, straight tube and a blockage, semicircular in cross-section, serving as a simplified model of an arterial stenosis. The stenosis is characterized by a single parameter, the aim being to highlight fundamental behaviours of constricted pulsatile flows. The Reynolds number is varied between 50 and 700 and the stenosis degree by area between 0.20 and 0.90. Numerically, a spectral element code is used to obtain the axisymmetric base flow fields, while experimentally, results are obtained for a similar set of geometries, using water as the working fluid. For low Reynolds numbers, the flow is characterized by a vortex ring which forms directly downstream of the stenosis, for which the strength and downstream propagation velocity vary with the stenosis degree. Linear stability analysis is performed on the simulated axisymmetric base flows, revealing a range of absolute instability modes. Comparisons are drawn between the numerical linear stability analysis and the observed instability in the experimental flows. The observed flows are less stable than the numerical analysis predicts, with convective shear layer instability present in the experimental flows. Evidence is found of Kelvin–Helmholtz-type shear layer roll-ups; nonetheless, the possibility of the numerically predicted absolute instability modes acting in the experimental flow is left open.

1. Introduction

There are numerous instances in the cardiovascular system in which fluid mechanical characteristics play a role in normal and pathological biological phenomena. For example, the appearance and growth of arterial blockages, or stenoses, has been linked to the presence of low and oscillatory wall shear stresses (Ku 1997). Such links have motivated researchers to examine the fluid mechanics associated with stenotic flows. A straight pipe with a partial blockage serves as a simplified model of an arterial stenosis, from which fundamental flow behaviours can be examined.

Early experimental work on pulsatile flows sought to identify flow disturbances which might provide indications of a stenosis (Cassanova & Giddens 1978). In particular, the work of Khalifa & Giddens (1978, 1981) characterized the change

---

† Email address for correspondence: martin.griffith@eng.monash.edu.au

in flow energy spectra with the severity of the stenosis. The work of Ahmed & Giddens (1984) moved away from turbulent flow energy spectra to the structure of the post-stenotic flow as a means to identify stenoses, using flow visualization techniques and laser Doppler velocimetry to extract downstream velocity profiles. The stenosis was modelled axisymmetrically, using a single cosine velocity wave form, with area reductions of 25 %, 50 % and 75 %. For the 75 % reduction, during the deceleration phase of the cycle, discrete oscillations in the near field flow and then turbulence approximately 6 diameters downstream of the stenosis were observed. It was concluded that the identification of flow disturbances such as those observed in their study were better indicators of stenosis severity than turbulent energy spectra derived from Doppler ultrasound techniques. However, no critical boundaries for the instabilities observed in their experiment were included.

Ohja *et al.* (1989) investigated post-stenotic pulsatile flow through two stenosis geometries, using a photochromatic tracer method. A single pulsatile wave form was used, and both stenosis geometries had sharp edges. The method was effective in delineating velocity profiles and also in indicating the breakdown of the flow in the post-stenotic region. A turbulent phase was identified, where the flow became turbulent around 5 diameters downstream of the stenosis, as well as a relaminarization phase, where the turbulence was convected downstream and where the jet emanating from the stenosis was stable and laminar. This observation of turbulence occurring only during a portion of the velocity wave form is common to other studies on pulsatile stenotic flow (Ahmed & Giddens 1984; Lieber & Giddens 1990; Ahmed 1998). For the turbulent phase of the 75 % area reduction, Ohja *et al.* (1989) divided the post-stenotic flow into regions, classifying each zone. In the stable jet region, three Kelvin–Helmholtz-type vortex roll-ups were observed. In the transition region, these roll-ups lost their symmetry, leading to their breakdown in the turbulent region. This turbulent region extended over the entire diameter of the tube and 3 diameters axially. The relaminarization of the flow occurred beyond 7.5 diameters downstream of the stenosis. The zone classifications give a good general characterization of an experimental pulsatile stenotic flow and are consistent with the observations regarding flow instability of Ahmed & Giddens (1984).

Many researchers have used computational fluid dynamics to investigate pulsatile flows in idealized stenotic geometries (Tu *et al.* 1992; Deplano & Siouffi 1999; Liu & Yamaguchi 2001; Varghese & Frankel 2003). Stroud, Berger & Saloner (2000) studied the influence of morphology on stenotic flows; their work also featured in the review paper of Berger & Jou (2000). The key motivation of the study seems to be to demonstrate the inadequacy of ‘percent stenosis’ as a diagnostic measure for arterial disease. This was achieved by investigating, independent of stenosis severity, the importance of such factors as surface irregularity and aspect ratio on flow behaviour. Many differences were found; however, the irregularities selected for the simulations seem fairly arbitrary. The work identified the significance of stenosis morphology but fell short of assessing or quantifying that significance.

More recently, the transition to turbulence observed in many stenotic flow experiments (Ahmed & Giddens 1984; Ohja *et al.* 1989) has been examined computationally. Simulating the pulsatile flow through an axisymmetric 75 % severity stenosis, Mallinger & Drikakis (2002) were able to recreate the downstream transition observed in previous experiments. Initially, the flow would remain laminar; the instability would then progress upstream and sit at a point downstream of the stenosis. The physical cause of this instability was not examined; however, the authors linked it to increases in the circumferential stress on the artery and larger-than-normal fluctuations of the wall shear stress. A qualitatively similar instability was also recreated and analysed by Sherwin & Blackburn (2005) in their simulations, using a geometry similar to that of Mallinger & Drikakis (2002).

The determination of critical Reynolds numbers or area reductions for instability is lacking from much of the work on stenotic flows; recently, the work of Sherwin & Blackburn (2005) and Blackburn & Sherwin (2007) has featured more in-depth stability analysis. Using Floquet stability analysis, Sherwin & Blackburn (2005) determined critical Reynolds numbers of pulsatile flow through a smooth cosine stenosis, similar to that used in Ahmed & Giddens (1984). For the greater part of the pulse period range relevant to physiological flows in large arteries, the primary linear instability in the flow was identified as a period-doubling vortex-tilting (azimuthal wavenumber $m = 1$). The instability acted on the vortex ring generated each pulse period, tilting each successive ring in opposite directions. Direct numerical simulation of the flow with a small flow perturbation added revealed the breakdown of the vortex rings far downstream, with an eventual relocation of this breakdown upstream, to within 4 diameters downstream of the stenosis. This asymptotic behaviour compares well with the instabilities described in the previous experimental work of Ohja *et al.* (1989) and Ahmed & Giddens (1984). However, the exact role of linear absolute instability modes in the stability of experimental flows is not determined, since the numerical simulations omit experimental noise, which may trigger substantial convective instability growth prior to criticality. In Blackburn & Sherwin (2007), different leading linear absolute instability modes were identified for flows of shorter pulse period, with modes of azimuthal wavenumber $m = 3$ and 4 dominating. The authors argued that they were Widnall instability modes (Widnall, Bliss & Tsai 1974), manifesting as azimuthal waves growing on each vortex ring.

Blackburn & Sherwin (2007) also investigated further the possibility of convective shear layer instability in pulsatile stenotic flow, adding a high-frequency, low-amplitude oscillation to the inlet velocity condition. They suggested a possible interaction between the convective shear layer instability and the linear Floquet instability. This took the study a step closer to the noise-driven instabilities seen in the experimental flows of Ahmed & Giddens (1984) and Ohja *et al.* (1989); however, the question of the exact role these linear instability modes might play in the experimental flows is still an open one.

Varghese, Frankel & Fischer (2007) have presented a detailed study of wall shear stress and velocity profiles for direct numerical simulations of pulsatile flow in an axisymmetric stenotic geometry of 75 % area reduction, using the same flow parameters and geometry used in Ahmed & Giddens (1984). They also performed simulations using the same stenosis model but with a geometric perturbation in the form of a 5 % eccentricity of the stenosis geometry. A comparison of velocity profiles between their simulations and the experimental measurements of Ahmed & Giddens (1984) showed a good agreement. They observed a breakdown of the post-stenotic flow in simulations performed with the stenosis of 5 % eccentricity, with periodic localized transitions (4 to 6 diameters downstream of the stenosis) to turbulence occurring during the deceleration phase of the wave form. In this way, the geometric eccentricity acted as a tripping mechanism for instability and turbulence rather than as an added flow perturbation (Sherwin & Blackburn 2005) or experimental noise (Ahmed & Giddens 1984; Ohja *et al.* 1989).

The present work aims to build on the recent computational work on pulsatile inlet stenotic flows, by providing experimental results for these flows as well as exploring the effect of a change in stenosis severity on the flow and its stability. The study is

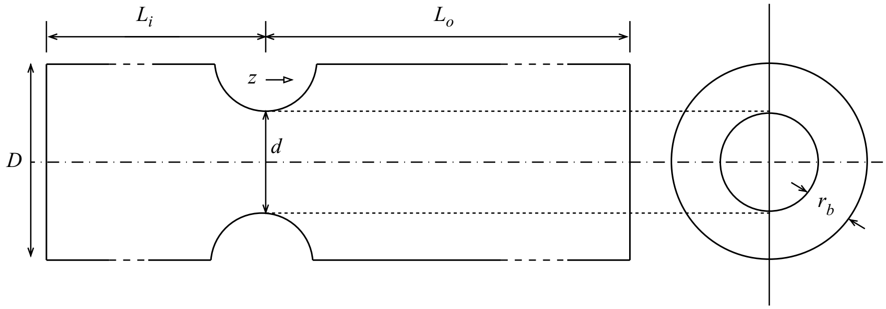

FIGURE 1. Schematic of the geometry.

a continuation of the work presented in Griffith *et al.* (2008), which dealt with the steady inlet flow through the same geometry.

This article is structured in the following manner: §2 describes the problem and outlines the numerical and experimental methods employed during the study; §3 presents the results, beginning with a description of the base flow and continuing to a description of the various flow instabilities investigated, while §4 summarizes the results and conclusions.

2. Problem definition and method

The geometry under investigation is shown in figure 1. It consists of a long, straight tube with an axisymmetric blockage described by a single parameter, the stenosis degree, defined as

$$b = 1 - \left(\frac{d}{D}\right)^2, \tag{2.1}$$

where D is the diameter of the tube and d is the diameter at the centre of the stenosis. Figure 1 also shows the radius of the blockage, dependent on d, which is given by

$$r_b = \frac{D-d}{2} = \frac{D}{2}(1-\sqrt{1-b}). \tag{2.2}$$

In actual blood flow, artery walls are generally compliant and respond to the fluid pressure and wall shear stresses. The walls of the tube of our model are considered to be rigid. As well as greatly simplifying our problem, the effect of compliant walls is generally considered negligible for the study of flows in larger arteries (Ku 1997; Wootton & Ku 1999). Similarly, for larger arteries it is reasonable to assume the fluid to be Newtonian.

The temporal and cross-sectional average of the fluid velocity, $\overline{U}$, is defined as

$$\overline{U} = \frac{1}{T_d}\int_0^{T_d} \overline{u}(t)\,\mathrm{d}t = \frac{8}{D^2 T_d}\int_0^{T_d}\int_0^{D/2} u(r,t)\,r\;\mathrm{d}r\,\mathrm{d}t, \tag{2.3}$$

where T_d is the period (dimensional) of the pulsation.

For a given wave form, three independent dimensionless parameters are defined: the Reynolds number, the pulse amplitude and the pulse period.

The Reynolds number is defined as

$$Re = \frac{\overline{U}D}{\nu}, \tag{2.4}$$

where ν is the kinematic viscosity.

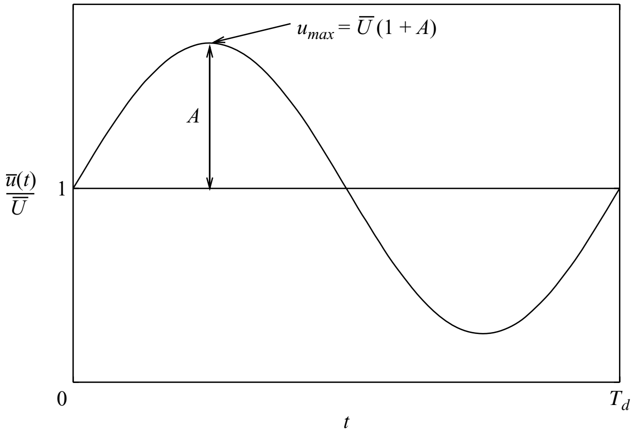

FIGURE 2. The inlet velocity waveform for pulsatile flow.

A sketch of the velocity wave form is given in figure 2. The sectionally averaged velocity oscillates sinusoidally around the temporally averaged flow velocity $\overline{U}$, with a period T_d and an amplitude A. The inlet flow produces the same net mass flow; the steady flow can be thought of as either a temporal average of the pulsatile flow or a limiting case, where the pulsation amplitude approaches zero. The amplitude, A, refers to the maximum variation of the velocity from its mean value of $\overline{U}$. As is the case in many other studies, the amplitude most often used in the present work is $A = 0.75$; this amplitude results in a wave form which oscillates between a maximum of $1.75\overline{U}$ and a minimum of $0.25\overline{U}$. Any wave form of amplitude $A > 1$ has a minimum velocity $\overline{u}(t)$ of less than 0, producing a reverse flow for a given interval of the pulse period.

The frequency parameter used is the non-dimensionalized period of the pulsation, $T = T_d\overline{U}/D$. In their work on pulsatile flows, Sherwin & Blackburn (2005) introduced a reduced velocity as a more suitable frequency parameter, which is in effect the same quantity as the non-dimensionalized pulsation period used in this study. In most previous works on pulsatile flow, the Womersley number ($\alpha = (D/2)\sqrt{2\pi/\nu T_d}$) is taken as the principal frequency parameter. The Womersley number is a useful indicator of the physiological relevance of any flow configuration one may be investigating; the equivalent Womersley numbers are provided for the flows considered in this study.

The study employs both numerical and experimental methods.

2.1. *Numerical simulations*

Two-dimensional axisymmetric flow field simulations were obtained from a numerical solution of the time-dependent Navier–Stokes equations, given here with the incompressibility constraint:

$$\frac{\partial \boldsymbol{u}}{\partial t} + \boldsymbol{u} \cdot \nabla \boldsymbol{u} = -\nabla \overline{p} + \nu \nabla^2 \boldsymbol{u}, \tag{2.5}$$

$$\nabla \cdot \boldsymbol{u} = 0, \tag{2.6}$$

where $\boldsymbol{u}$ is the three-dimensional velocity vector (solved axisymmetrically) and $\overline{p}$ and ν are the kinematic pressure and viscosity. The simulations were initialized with the fluid at rest and run until the flow had travelled the length of the domain. The spectral element method employed to discretize and solve the equations has been used and validated in the prediction of wake flows past rings (Sheard, Thompson & Hourigan 2003), spheres (Thompson, Leweke & Provansal 2001), circular cylinders (Thompson, Hourigan & Sheridan 1996) and partial blockages in channel flow (Griffith *et al.* 2007). The method uses a three-step time-splitting procedure and has been verified to give second-order time accuracy.

2.1.1. *Boundary conditions*

On the stenosis surface and the cylinder walls, no-slip conditions were imposed. At the inlet and outlet boundaries, the pulsatile inlet condition is prescribed, consisting of a linear combination of an equilibrium Poiseuille profile and a harmonic oscillation. The solution to the harmonic component of the velocity is given in Womersley (1955). A thorough discussion of the Womersley solution and the resulting velocity profile behaviour can be found in Loudon & Tordesillas (1998). The Womersley solution represents a fully developed and periodic solution for flow subject to a periodic pressure gradient. The time-dependent complex solution to the local velocity for pulsatile flow is given by (9) of Womersley (1955) as

$$u(r,t)=\frac{A}{\rho}\frac{T_d}{2\pi i}\left(1-\frac{J_0(2\alpha r i^{3/2}/D)}{J_0(\alpha i^{3/2})}\right)\exp 2\pi i t/T_d, \tag{2.7}$$

where A is the magnitude of the pressure gradient; $i=\sqrt{-1}$; and J_0 represents a complex Bessel function of order zero. The resultant harmonic component can then be added on to the mean steady component.

2.1.2. *Stability analysis*

Floquet stability analysis is carried out on the numerically simulated flows. The method analyses the linear growth, or decay, of a perturbation, $\mathbf{u}'(r,\theta,z,t)$, on the periodic base flow, $\boldsymbol{u}(r,\theta,z,t)$. Describing the flow as the base and perturbation components combined, this definition is substituted into the Navier–Stokes equations. Subtracting the base flow components and removing nonlinear terms yields linear equations describing the evolution of small disturbances, which can be solved by the same numerical method used to solve the base flow. For a given azimuthal wavenumber, m, a Floquet multiplier μ is determined by the power method. A Floquet multiplier $|\mu|>1$ indicates an unstable flow, while $|\mu|<1$ indicates a stable one. A Floquet multiplier $|\mu|=1$ represents neutral stability; in such a case the flow is of a critical Reynolds number Re_c for perturbations of the particular wavenumber, above which it is stable and below which it is unstable. The method is the same one used in Griffith *et al.* (2007), only modified for axisymmetric configurations and periodic base flow; hence the mathematical details are not provided here.

2.1.3. *Mesh layout and validation*

Meshes were created for stenosis degrees of $b=0.20$, 0.40, 0.50, 0.60, 0.75 and 0.90. For the mesh constructed corresponding to a stenosis degree $b=0.90$, a much higher spatial and temporal resolution than for the steady flow case was needed to adequately resolve the flow. Therefore, simulation of pulsatile flows at $b=0.90$ required much longer computational times than those at lower stenosis degrees. Due to the prohibitive computational time needed, only a limited number of flow configurations were simulated at $b=0.90$; these were mostly chosen to compare with configurations tested experimentally.

Figure 3 shows three of the meshes used. The inlet length used for all meshes was $L_i=6D$, while the outlet length L_o varied according to the stenosis degree. At low stenosis degree, the outlet length used was $40D$, increasing to $50D$ at $b=0.60$, $75D$

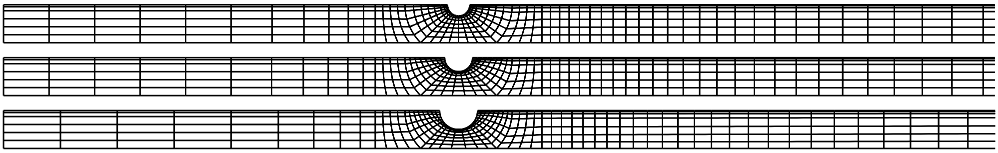

FIGURE 3. Macro-elements for test sections of three of the meshes constructed. From top to bottom, $b = 0.50$, 0.60 and 0.75.

n	$b = 0.50$ $\lvert\mu\rvert$	$b = 0.60$ $\lvert\mu\rvert$	$b = 0.75$ $\lvert\mu\rvert$
3	1.0835	1.2546	–
4	1.1529	1.3640	1.8777
5	1.1726	1.3763	1.4898
6	1.1725	1.3763	1.4953
7	1.1728	1.3765	1.4942
8	1.1716	1.3761	1.4940
9	1.1708	1.3761	1.4948

TABLE 1. Convergence of the Floquet multiplier, μ, with polynomial order, n, for the azimuthal wavenumber $m = 1$ mode, across three stenosis degrees. All three tests were performed with $Re = 300$ and $T = 2.5$ and with an amplitude of pulsation exceeding the critical pulsation amplitude (i.e. at $b = 0.50$, $A = 1.25$; at $b = 0.60$, $A = 1.00$; and at $b = 0.75$, $A = 0.75$).

at $b = 0.75$ and $100D$ at $b = 0.90$. These lengths were found to be sufficient to remove any artificial boundary effects from either the inlet or the outlet.

The results of a resolution study are shown in table 1. The absolute value of the Floquet multiplier of the leading azimuthal mode in each case was chosen as the most convenient characteristic with which to measure the convergence. The three cases shown were conducted for $Re = 300$ and $T = 2.5$ and then with a pulse amplitude, A, taken from the higher end of the range of values studied. The convergence in each case is good, each multiplier at the maximum nodal concentration being within 0.2 % of the multiplier calculated at $n = 6$. All the pulsatile flows simulated in this study were obtained using a nodal concentration of 49 (7×7) nodes per element, or $n = 7$. For the case corresponding to $b = 0.75$ from table 1, the effect of a variation in the time step was tested. Simulations run at time steps of $\Delta t\overline{U}/D = 2.5 \times 10^{-4}$, 2.0×10^{-4} and 1.0×10^{-4} produced a variation in the value of $|\mu|$ of less than 0.2 %.

2.2. *Experimental method*

An experimental rig was constructed to test the geometry outlined in figure 1. A schematic of the rig design is shown in figure 4. A brief description of the rig is presented here, although a more detailed description is available in Griffith (2007). The rig consisted of a transparent perspex tube of 20 mm diameter, with inlet and outlet lengths of 2000 mm or $100D$. This provided a fully developed Poiseuille flow at the test section and restricted any end effects. The three removable test sections constructed corresponded to stenosis degrees of $b = 0.50$, 0.75 and 0.90. The test section and outlet length were contained in a water-filled rectangular viewing box, allowing the flow to be viewed undistorted; however, the curvature of the tube led to some laser reflections which interfered with the view of the flow near the sections of the tube wall normal to the viewer (the top and bottom of the experimental section).

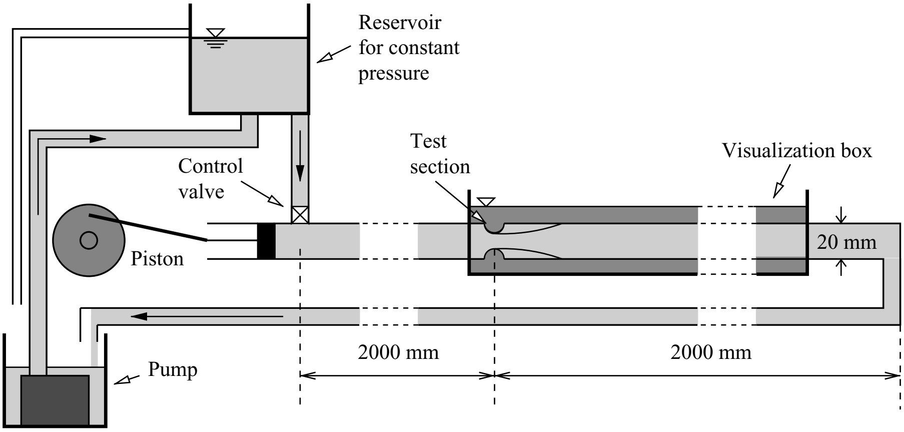

FIGURE 4. Schematic of the experimental rig; the inlet and outlet lengths have been truncated.

A pump supplied an elevated water reservoir, thereby keeping the pressure in the system constant. The Reynolds number was varied via a control valve located before the entry into the inlet tube.

A piston was added at the junction immediately downstream of the control valve. This piston allowed the investigation of flows subject to a large-amplitude periodic pulse. At running conditions, the pressure drop across the control valve was very large, thus ensuring that movement from the piston was translated directly downstream and only a negligible portion lost upstream to the reservoir. Much effort was invested in reducing the noise and vibration in the system: the water pump and piston were isolated as much as possible with the straightness of the tube ensured and filters placed to smooth the flow before its entry into the inlet section. A turbulence intensity of 3.0 % in the upstream (unblocked) flow was measured. Another source of error stems from temperature differences existing between the working fluid and fluid in the visualization box. Large differences between these two fluids could significantly distort the flow in the tube. To minimize this effect, the fluid of the visualization box was incorporated into the flow circuit of the experiment, generating a gentle flow through the box, thereby keeping the fluids at approximately the same temperature.

The flow was analysed primarily using coloured dye visualizations. Fluorescein dye was injected into the flow – with steady inlet condition – immediately downstream of the stenosis, allowed to settle and then illuminated by a laser sheet. Dye would become trapped in a steady recirculation zone. At this point, the pulsation would begin, the dye from the recirculation zone of the steady flow serving to visualize the pulsatile flow. The exact phase of single images was not determined; however, knowing the exact period of the flow, the phase of an image could be determined in its relation to another. In each figure showing series of dye visualizations, the first image is given an indeterminate time t_i, which serves as a reference for later images in the figure ($t_i + T/8$, $t_i + 2T/8$ and so forth).

Particle image velocimetry (PIV) was also employed to measure the mainstream flow; a detailed description of the technique and software used can be found in Meunier & Leweke (2003). The results presented in this paper were obtained from ensemble averaging; interrogation windows were also given a 4:1 aspect ratio, to reflect the generally higher streamwise velocity component of the fluid flow. It was found that the particle density was lower in the flow close to the tube walls than in

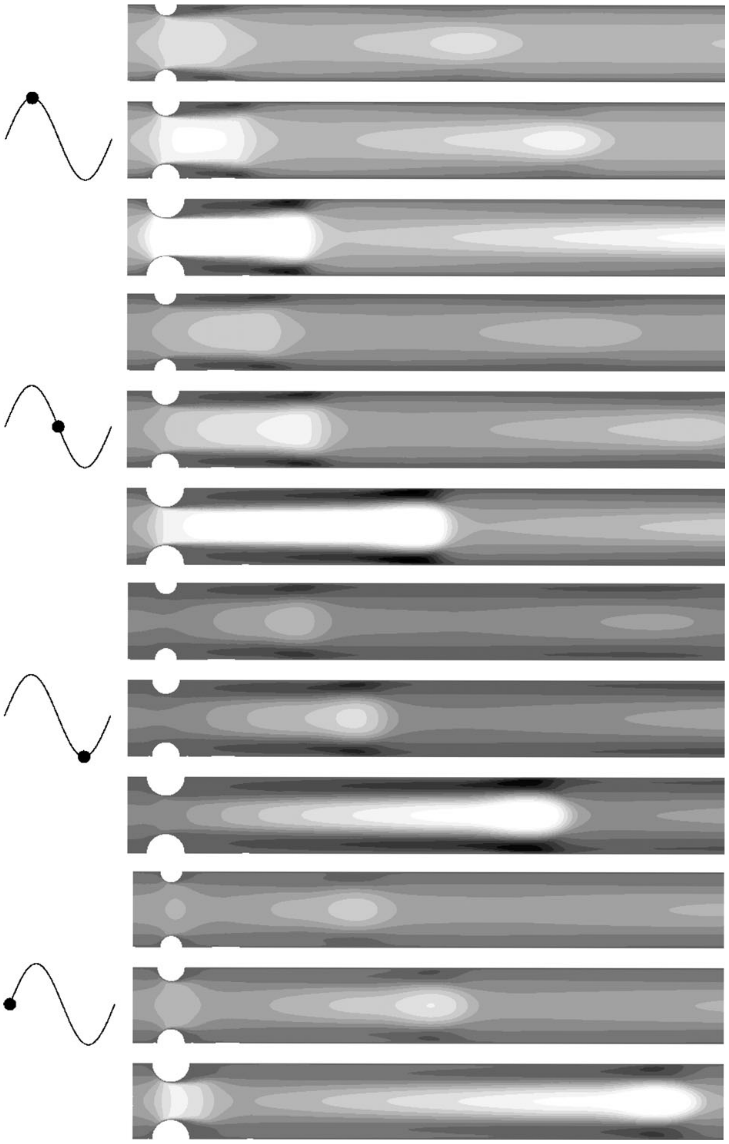

FIGURE 5. Contours of axial velocity of the flow through four stages of the pulse, at $T = 2.5$ ($\alpha = 13.73$), $Re = 300$ and $A = 0.75$, across three stenosis degrees, $b = 0.50$, 0.60 and 0.75. In each image, 10 contours are shown, between $u = 0$ and $5\overline{U}$.

the centre of the tube; this tendency of the imaging particles resulted in the technique not being as accurate in the near-wall vicinity.

3. Results

3.1. *Base flow dynamics*

Figure 5 plots contours of axial velocity obtained from numerical simulations up to an axial distance of $z/D = 7$ for $Re = 300$ and $T = 2.5$, across three stenosis degrees $b = 0.50$, 0.60 and 0.75. The flow configuration serves here as a generic example of

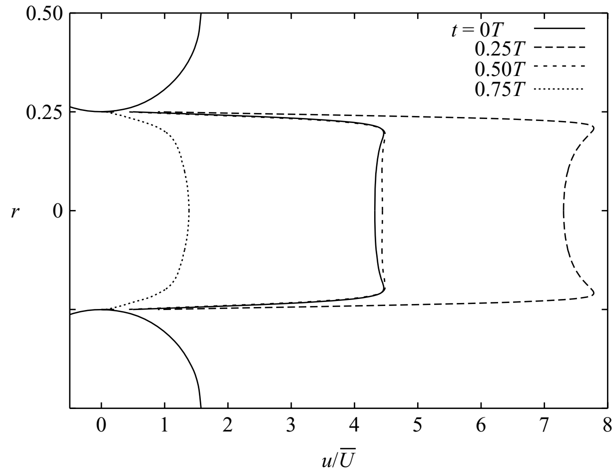

FIGURE 6. Axial velocity profiles in the contraction of the $b = 0.75$ geometry at four intervals during the pulse period, with $Re = 300$, $A = 0.75$ and $T = 2.5$ ($\alpha = 13.73$).

the types of flow under question, and the four sets of images are ordered in such a way as to show the development and propagation of the flow during one period. The Womersley number in this case, $\alpha = 13.73$, is in the range corresponding to large arteries.

At $t = 0.25T$, when the sectionally averaged velocity is at a maximum, the flow acceleration from the velocity wave form and the stenosis combined produce a plug of high axial velocity, issuing from the contraction. The acceleration is markedly stronger at $b = 0.75$, the velocity within the contraction being 4 times greater ($1/(1 - b)$) than the velocity in the unblocked tube. The corresponding ratios for $b = 0.50$ and 0.60 are 2 and 2.5, respectively. This bulge of high-velocity fluid continues downstream during the period of pulsation; during the same period, the bulk fluid itself moves $2.5D$ downstream.

In order to further analyse the plug-like form of the flow through the contraction, figure 6 shows plots of the velocity profiles for the same flow configuration and intervals in the period as in figure 5; however, only the case with $b = 0.75$ is considered. Here, the axial velocity takes a local maximum near the inside walls of the stenosis. For $t = 0.25T$, when the sectionally averaged velocity inside the contraction reaches its maximum of $\overline{u}(t) \approx 7\overline{U}$, the maximum is even more pronounced. The higher axial velocity near the walls is caused by the rapid contraction of the flow and then accentuated by the acceleration in the velocity wave form. The profiles of the two other phases presented, $t = 0.5T$ and $0.75T$, occur during the diastolic portion of the wave form, and the profiles become more rounded. In other studies that use a stenosis length of $2D$ for a stenosis degree of $b = 0.75$ (as opposed to a length of $0.5D$ for the present geometry at $b = 0.75$), the local maximum is either not present or not as pronounced.

The separating shear layer can be observed in figure 7, which presents contours of vorticity for the same flow configuration as in figure 5, with $Re = 300$ and $T = 2.5$, across three stenosis degrees, $b = 0.50$, 0.60 and 0.75. The strong flow acceleration through the stenosis causes a flow separation to occur, with a separating shear layer emanating from the blockage walls. The shear layer rolls up, forming a vortex ring which propagates downstream and leaves a trail of positive vorticity in its wake.

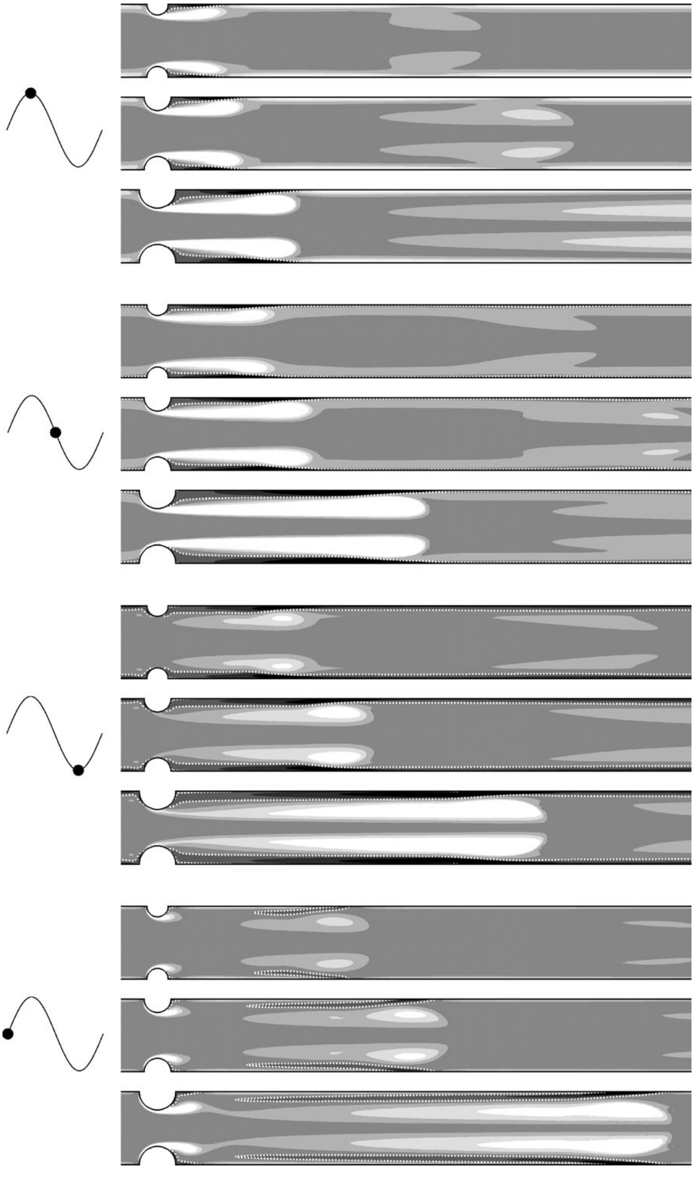

FIGURE 7. Contours of azimuthal vorticity of the flow through four stages of the pulse, at $T = 2.5$ ($\alpha = 13.7$), $Re = 300$ and $A = 0.75$, for three stenosis degrees, $b = 0.50, 0.60$ and 0.75. Dashed white lines represent the contour $\omega_\theta = 0$; eight contour levels are shown, for $-20\overline{U}/D \leqslant \omega_\theta \leqslant 20\overline{U}/D$.

As can be seen from figures 7 and 11, the strength and extent of convection downstream of the vortex are much greater in the case of $b = 0.75$. The vortex moves at a velocity closer to the heightened mean velocity inside the stenosis rather than at the mean velocity of the unblocked tube.

3.1.1. *Vortex ring behaviour*

The variation of the propagation of the vortex downstream warrants further investigation. Figure 8 plots the axial distance covered by the vortex as a function

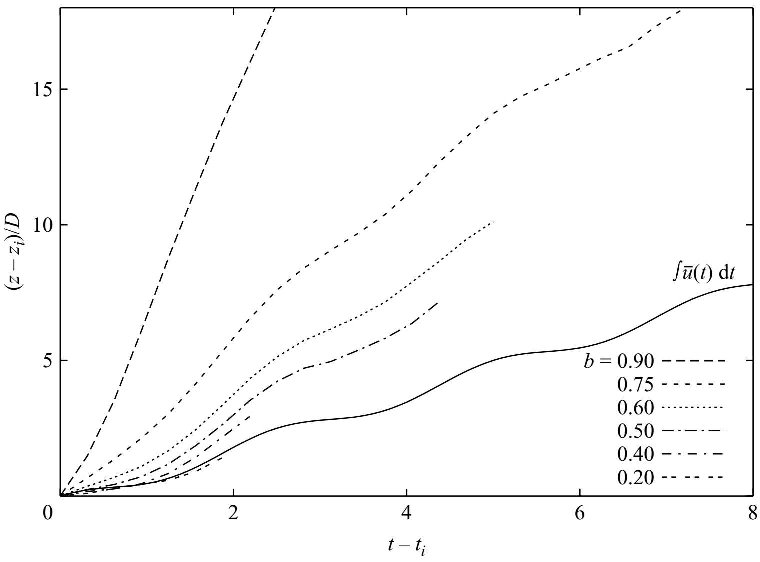

FIGURE 8. The position downstream of a vortex, as a function of time, for $T = 2.5$ ($\alpha = 13.73$), $Re = 300$ and $A = 0.75$, across the stenosis degree range. The solid line indicates the position travelled by a particle should it convect with the sectionally averaged axial velocity, $\overline{u}(t)$.

of time, for each of the stenosis degrees tested; z is the distance downstream of the stenosis, while z_i is the z-position of the vortex at $t = t_i$. In each case, the measurements were begun at the same phase. For $b = 0.20$, the vortex ring follows the sectionally averaged velocity in the tube, $\overline{u}(t)$, for the duration of its relatively short existence. A stenosis degree of $b = 0.20$ corresponds to a stenosis which extends only $0.053D$ into the tube, so only a relatively minor effect on the mainstream flow is to be expected. For stenosis degrees of $b = 0.40$ and greater, the vortex rings travel faster than the sectionally averaged velocity. The vortex ring velocity, excluding the effect of the sinusoidal variation of the mean velocity in the tube, seems to be constant. While the mean velocity in the tube obviously has an effect on the vortex position – evident in the undulations of the curves – the difference between the downstream velocity of the vortex ring and the mean velocity in the tube must be a result of its circulation, which would be a function of the increased velocity through the contraction and, therefore, of the stenosis degree.

The vortex ring axial velocity can be calculated immediately downstream of the stenosis, independent of the oscillating mean velocity in the tube, by using the two axial positions of the ring at $t - t_i = 0$ and $t - t_i = 2.5$. For the case of $b = 0.40$, the position of the vortex at $t - t_i = 2.5$ is extrapolated from the axial position at which it dissipates and is no longer observable. Doing so, it is found that at $b = 0.75$, the vortex travels at a speed of approximately $3\overline{U}$; this compares with a speed of $\sim 2\overline{U}$ at $b = 0.60$ and $\sim 1.7\overline{U}$ at $b = 0.50$. Given that the downstream velocity of the vortex ring seems to be a function of the circulation imparted through the stenosis, the vortex ring velocity is normalized by $1/(1 - b)$; this quantity is the factor by which the sectionally averaged velocity is increased inside the contraction. This rescaled value of vortex ring axial velocity V_v is plotted in figure 9 for stenosis degrees of 0.20 to 0.90. A small extrapolation was required for $b = 0.40$, while a much larger extrapolation was required for $b = 0.20$. The vortex ring velocity trend at $b = 0.20$ seems to be markedly different than that of the other stenosis degrees. Examining again figure 8,

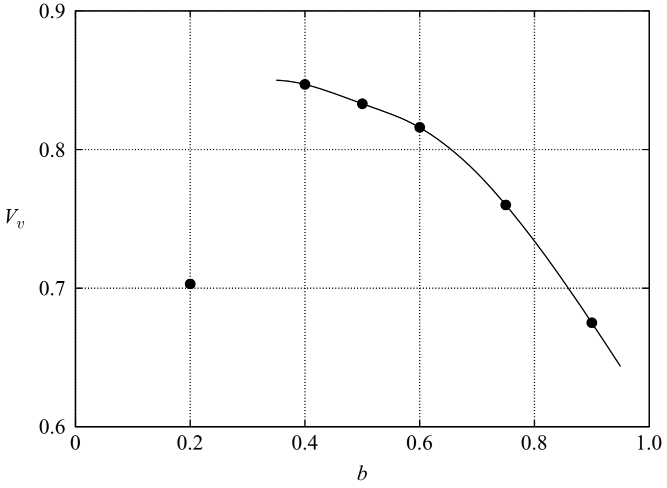

FIGURE 9. Values of rescaled vortex ring axial velocity, V_v, against stenosis degree, for $Re = 300$, $T = 2.5$ and $A = 0.75$.

for $b = 0.20$, the vortex ring appears to travel slower than the sectionally averaged fluid velocity and only exists for a short time. Again, the extremely small size of the blockage may account for the weaker, slower vortex rings seen for $b = 0.20$. As b approaches zero, the blockage moves deeper into the boundary layer, and the velocity over the stenosis decreases, which would have an effect on the formation of the vortex ring.

For b greater than 0.20, V_v decreases as b increases. This variation in V_v is the same at pulse periods $T = 1.0$ and 5.0. A possible explanation for this decrease is the fact that a newly generated vortex ring in the geometry $b = 0.75$ travels much further downstream during the pulse period than in lower stenosis degree geometries. In convecting downstream at a higher velocity, the vortex may be subject to a greater viscous drag from the tube wall than a vortex generated in a geometry of lower stenosis degree. Another explanation lies in the amount of circulation imparted to the vortex, as compared to the acceleration through the contraction. The axial velocity, V_v, of the vortex is due chiefly to the circulation of the vortex, which it gathers during its formation. Examining again the vorticity contours of figure 7, it is seen that for $b = 0.75$, a large trail of vorticity is left in the wake of the vortex. This trail reduces in size at $b = 0.50$ and 0.60; the size of the trail in proportion to the strength of the vortex also appears to be smaller, particularly in the fourth panel, which corresponds to the phase interval $t = 1.0T$. The lower value of V_v for $b = 0.75$ perhaps indicates a higher proportion of the acceleration through the contraction ending up in the wake of the vortex ring rather than as circulation within the vortex ring.

By investigating the flow generated by the motion of a piston into an unbounded domain, Gharib, Rambod & Shariff (1998) showed that a vortex ring can take up only a certain quantity of circulation during its formation before it pinches off, detaching itself from the separating shear layer feeding it. Any excess circulation generated by the piston is left in a trail of vorticity behind the vortex. This behaviour bears some resemblance to the behaviour of the stenotic flows under investigation here.

The chief difference is in the shape of the vortex ring; it is elongated with the axial direction of the flow, necessarily due to the presence of the tube walls. Considering the vortex rings used in the study of Gharib *et al.* (1998) – which act in an unbounded domain – the vortex has a greater lateral expansion than in the present work. In the tubular geometry, the vortex is severely constricted and not able to develop and propagate in the same manner. Qualitatively, the same physical phenomenon is present, whereby a vortex ring, attaining a certain circulation threshold, detaches from the separating shear layer, travels downstream and leaves a trail of vorticity in its wake. This explanation is further supported by the drop in normalized vortex ring axial velocity, V_v, with increasing stenosis degree, a phenomenon which can be explained by the greater proportional quantity of circulation deposited in the vortex trail.

3.1.2. *Wall shear stresses*

The wall shear stress, $\tau_{wall} = -\rho\nu\partial u/\partial r$, has been established as the primary fluid mechanical characteristic affecting biological arterial responses (Ku 1997; Wootton & Ku 1999). Figure 10 plots profiles of wall shear stress along the tube wall, for $b = 0.75$, $Re = 300$, $A = 0.75$, for three different pulse periods $T = 1.0$, 2.5 and 4.0 ($\alpha = 21.71$, 13.73 and 10.85). Wall shear stress is normalized as

$$\tau = \tau_{wall} \bigg/ \left(\frac{1}{2}\rho\overline{U}^2\right) = -\left(\frac{2D}{Re\overline{U}}\right)\frac{\partial u}{\partial r}. \tag{3.1}$$

Twenty profiles over one pulse period are shown, the intention being to delineate an envelope within which the wall shear stress oscillates. The data sets shown begin at the axial location $z = r_b$ or where the stenosis ends. The first case, for $T = 1$, having a Womersley number of 21.73, models a flow configuration similar to that of a large artery close to the heart, while the second and third cases are still characteristic of large arteries but further away from the heart. At smaller pulsation periods, greater maximum shear stresses and amplitudes of oscillation are observed than for higher pulsation periods. As the three cases involve pulsations of the same amplitude, the rate of change of the sectionally averaged fluid velocity is necessarily greater for shorter pulse periods, which in turn leads to increased velocity and, accordingly, increased wall stress. In the three cases, the wall shear stress reaches a maximum just downstream of the stenosis, with the maximum shifting downstream as the pulse period is increased.

The wall shear stress corresponding to the steady inlet flow and the average wall shear stress of the pulsatile flow for $Re = 300$ are also plotted in figure 10. For $T = 2.5$ and 4.0, the average wall shear stress becomes positive at approximately the same point at which the wall shear stress switches sign in the steady inlet flow or where the recirculation zone formed in the steady flow ends. However, in the case of $T = 1.0$, the average wall shear stress exhibits a distribution different from that of the steady flow: immediately downstream of the stenosis, the average wall shear stress is positive. The explanation for this behaviour lies in a particular vorticity field topology which emerges for shorter pulse periods.

Figure 11 plots vorticity contours of the flow for the same parameters as for figure 7, only with pulse period $T = 1.0$. In comparison with the flows of figure 7, the most obvious difference is the shorter axial distance between each successive vortex ring. However, observing the wake of the vortex ring just downstream of the blockage, in each case one finds a small thread of negative vorticity which lifts away and approaches the centreline of the tube, with a region of positive vorticity remaining on the wall. This is in contrast to the flow for $T = 2.5$, where the negative vorticity surrounding the main vortex ring remains attached to the wall. In the velocity plots (not shown) of these flows at $T = 1.0$, this feature of the flow manifests as a local

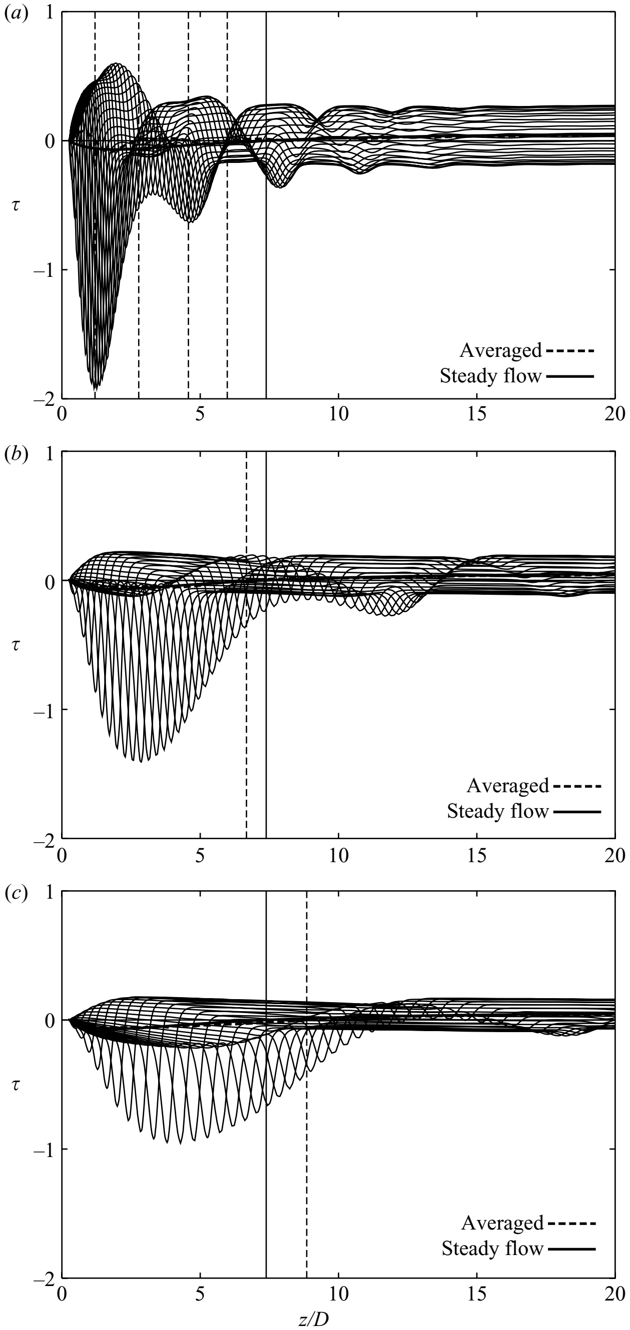

FIGURE 10. Variation of wall shear stress, τ, over one pulse period, for (*a*) $T = 1.0$, (*b*) $T = 2.5$ and (*c*) $T = 4.0$, with $Re = 300$, $b = 0.75$ and $A = 0.75$. The graphs, in effect, show envelopes of shear stresses at given axial locations. The heavy dashed line indicates the wall shear stress averaged over one pulse period, while the solid heavy line indicates the wall shear stress distribution for steady flow at the same Reynolds number; vertical lines indicate where the wall shear stress changes sign. The Womersley number values are $\alpha = 21.71$, 13.73 and 10.85 respectively.

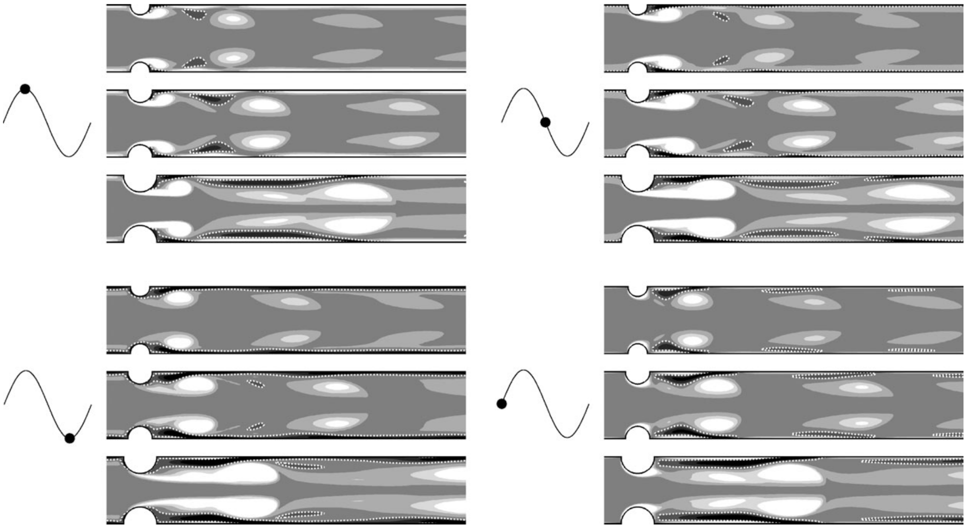

FIGURE 11. Contours of azimuthal vorticity of the flow through four stages of the pulse, at $T = 1.0$ ($\alpha = 21.7$), $Re = 300$ and $A = 0.75$, for three stenosis degrees, $b = 0.50, 0.60$ and 0.75. Dashed white lines represent the contour $\omega_\theta = 0$. Contours are the same as in figure 7; that is eight levels for $-20\overline{U}/D \leqslant \omega_\theta \leqslant 20\overline{U}/D$.

maximum of axial velocity near the wall, just upstream of the main vortex ring. This difference in the topology of the vorticity fields for the flows of period $T = 1.0$ accounts for the positive average wall shear stress distribution downstream of the blockage in figure 10(*a*).

Figure 12 tracks the wall shear stress as it varies from a stenosis degree of $b = 0.40$ to $b = 0.75$, for Reynolds number $Re = 300$ and pulsation period $T = 2.5$. In each of the four cases presented, the wall shear stress achieves a maximum local value, in absolute terms, a short distance downstream of the stenosis. This maximum local wall shear stress grows sharply with stenosis degree, reaching a value for $b = 0.75$ of approximately five times that for $b = 0.40$. From figure 12(*a*), for $b = 0.40$, the effect of the stenosis on the variation of the wall shear stress is relatively small and extends only a short distance downstream of the stenosis. This is particularly the case if the wall shear stress is considered in terms of the range of values it oscillates within. Approximately 8 diameters downstream of the stenosis, the wall shear stress oscillation has almost returned to its standard envelope of oscillation in an unblocked tube. It is only for $b = 0.75$ that the effect of the stenosis begins to substantially penetrate downstream, with the oscillation disrupted at least up to $z = 20D$. In addition, the maximum value of local shear stress achieved during one period is shifted a short distance downstream.

3.1.3. *Experimental validation*

For an unblocked tube – or a section upstream of the stenosis – figure 13(*a*) plots a comparison over one pulse period between the analytical Womersley solution for the velocity, $u(r, t)$, and values measured experimentally using PIV, for $Re = 190$, $A = 0.75$ and $T = 1.75$. The values are phase-averaged over 10 pulsation periods. The agreement is good, excepting values closer to the tube walls. PIV analysis was hampered by difficulties associated with the curvature of the tube: reflections of the laser, particularly on the bottom half of the tube, led to a loss of information near the

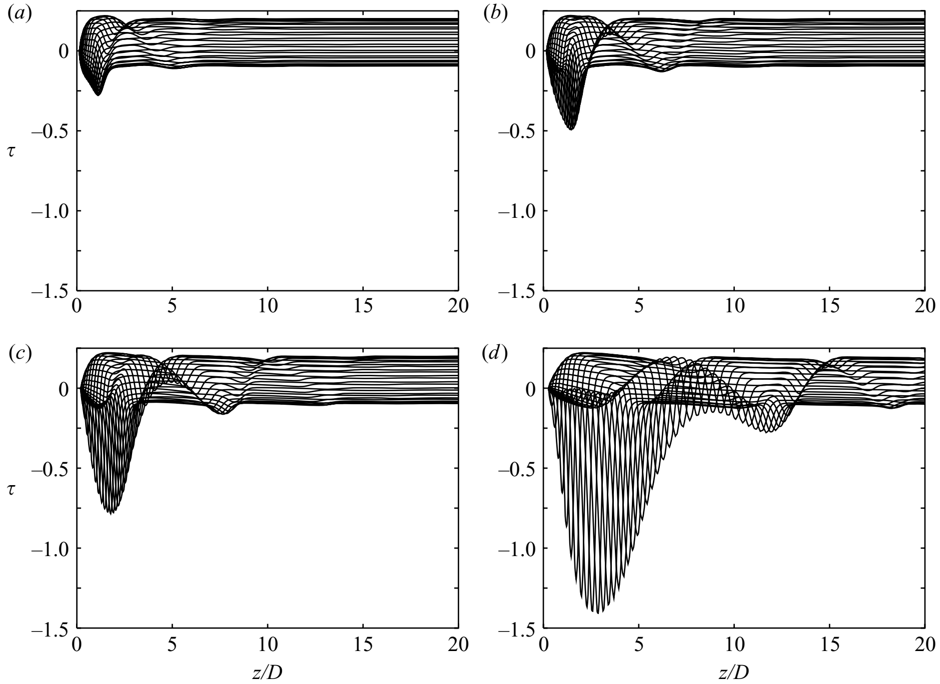

FIGURE 12. Variation of wall shear stress, τ, for stenosis degrees of (*a*) $b = 0.40$, (*b*) $b = 0.50$, (*c*) $b = 0.60$ and (*d*) $b = 0.75$ over one pulse period, for $T = 2.5$, $Re = 300$ and $A = 0.75$. The graphs show envelopes of shear stresses at given axial locations. The Womersley number is $\alpha = 13.73$.

bottom and top edges of the flow field under investigation. Also, the particle density of the fluid near the walls was found to be not as great as in the mainstream flow. The same measurements are plotted in figure 13(*b*) as figure 13(*a*) but averaged over the cross-sectional area of the tube, thus giving the sectionally averaged velocity, $\overline{u}(t)$. The agreement of figure 13(*b*) is good, indicating the period and amplitude of the created pulsation are reasonably accurate.

Comparisons of a numerical simulation with corresponding PIV-measured velocity fields are shown in figure 14, for $b = 0.50$, $Re = 315$, $A = 0.75$ and $T = 3.92$. The PIV measurements are averaged over 10 pulse periods. The phase is determined by integrating $u(r, t)$ at an axial location to obtain $\overline{u}(t)$, from which the position along the velocity wave form can be determined.

For this flow configuration, Floquet stability analysis predicts the flow to be stable, $Re = 315$ being approximately half the critical Reynolds number expected (figure 15*a*). The experimental measurements also show the flow to be stable; the formation of the vortex ring can be discerned, as well as its progression downstream. The vortex can be detected until the end of the field of vision at $z/D = 6.0$. The vorticity is well matched between the two data sets.

3.2. *Flow stability*

3.2.1. *Floquet stability analysis*

Floquet stability analysis on the numerical simulations allows us to determine critical Reynolds numbers for the linear stability of the flows under investigation. Figure 15 plots a summary of critical Reynolds numbers across a range of pulse

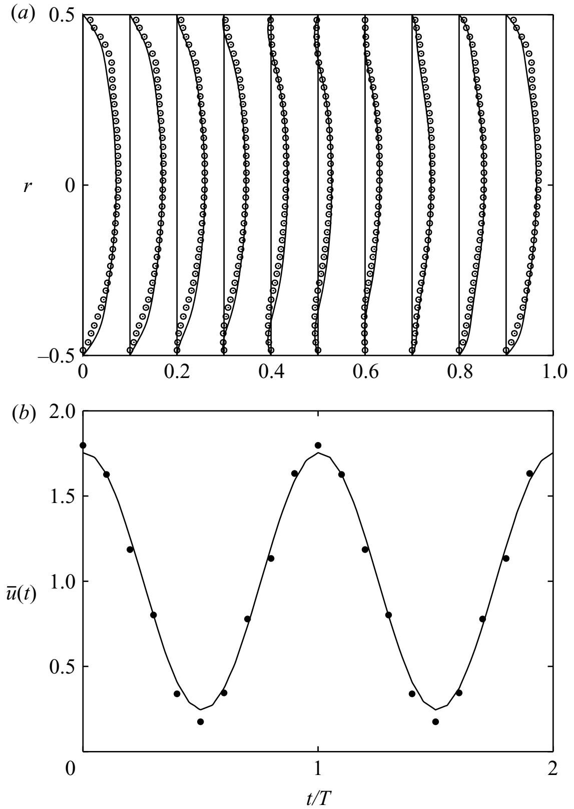

FIGURE 13. (*a*) Comparison of velocity profiles over one pulse period between PIV data (circles) and numerical data (lines) in an unblocked channel and (*b*) comparison of the sectionally averaged velocity, $\bar{u}(t)$, over two pulse periods, for $Re = 190$, $A = 0.75$ and $T = 1.75$ ($\alpha = 13.06$) for PIV data (dots) and numerical solution (line). PIV data are phase-averaged over 10 pulsation cycles.

periods and three stenosis degrees, $b = 0.50$, 0.60 and 0.75. The figure plots the boundaries at which the various instability modes become critical. The modes depicted exhibit critical Floquet multipliers of both 1 and −1. A positive Floquet multiplier indicates a perturbation which has the same period as the base flow. In contrast, a negative Floquet multiplier indicates a period-doubling instability, where the sign of the azimuthal vorticity of the perturbation mode changes from one period to the next. In effect, this means that the sign of the perturbation switches from one downstream vortex ring to the next. Period-doubling modes are indicated in the figure by hollow symbols. Solid symbols indicate modes of real and positive Floquet multiplier.

For the stenosis degrees tested, at the higher end of the pulse period range, a period-doubling bifurcation of azimuthal wavenumber $m = 1$ dominates. An example of the mode is presented in figure 16, where the axial vorticity of the perturbation mode for $b = 0.50$, $Re = 500$, just above the critical Reynolds number, is plotted. The maximum perturbation is centred around the vortex ring. For the case shown for the stenosis degree $b = 0.50$, the perturbation is first evident at $z/D \approx 8$. At this point, the top half of the vortex ring is subject to a tilting in one axial direction, while the bottom half is tilted in the other. The orientation of the tilting alternates on each vortex, which is evident by the change in sign of the perturbation vorticity on each

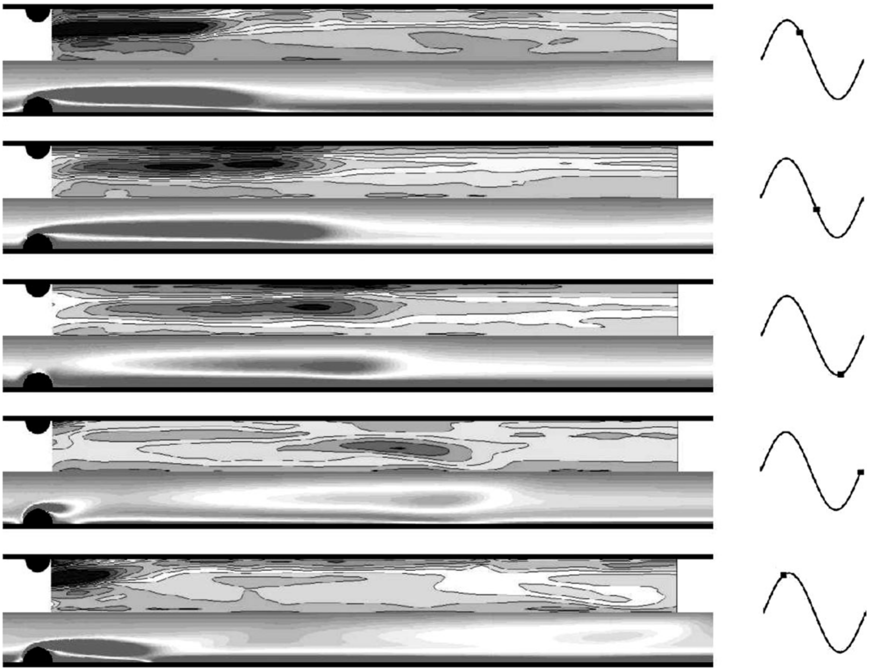

FIGURE 14. Contours of azimuthal vorticity of a comparison of PIV (top halves) with numerical simulations (bottom halves), over one period, for $b = 0.50$, $Re = 315$, $A = 0.75$ and $T = 3.92$ ($\alpha = 11.23$). Experimental flow fields are phase-averaged over 10 pulsation periods.

successive base flow vortex ring. In each of the three cases, the $m = 1$ mode has an optimum period, in which the critical Reynolds number is at its lowest. This optimum pulse period increases slightly for lower stenosis degrees.

For the other two stenosis degrees tested, in addition to the $m = 1$ sub-harmonic vortex-tilting perturbation mode, a number of other modes become dominant for other pulse periods. For $b = 0.50$ and 0.60, a sub-harmonic mode of wavenumber $m = 2$ is dominant for the pulse period ranges $1.4 \lesssim T \lesssim 2.2$ and $1.1 \lesssim T \lesssim 1.6$, respectively. At still lower pulse periods, for $b = 0.50$, a sub-harmonic mode of wavenumber $m = 3$ dominates, while for $b = 0.60$, a harmonic mode of wavenumber $m = 6$ takes over.

Figure 17 plots an example of one of these lower range pulse period modes; contours of the axial velocity of the base flow, along with contours of the axial vorticity of the leading perturbation mode, $m = 6$, for $b = 0.60$, $T = 1.0$ and Reynolds number $Re = 480$ – just above the critical Reynolds number, $Re_c = 479$ – are depicted. The perturbation grows immediately downstream of the stenosis; the vorticity appears to grow on the vortex under formation in the throat of the contraction and interact with the next vortex downstream, where the perturbation vorticity is at its greatest, $z/D = 1.85$ (and where the cross-sectional slice of figure 17*c* is taken). The perturbation mode grows immediately downstream of the stenosis.

A second mode observed for pulse period $T = 1.0$ is that of wavenumber $m = 3$ for $b = 0.50$; figure 18 shows plots of the base flow and perturbation mode for $Re = 575$. Although not discernible from the figure, the perturbation vorticity reaches a maximum at $z/D \approx 7$. The perturbation vortex structure becomes elongated as it travels downstream, dissipating as the base flow vortex ring dies away. There is no

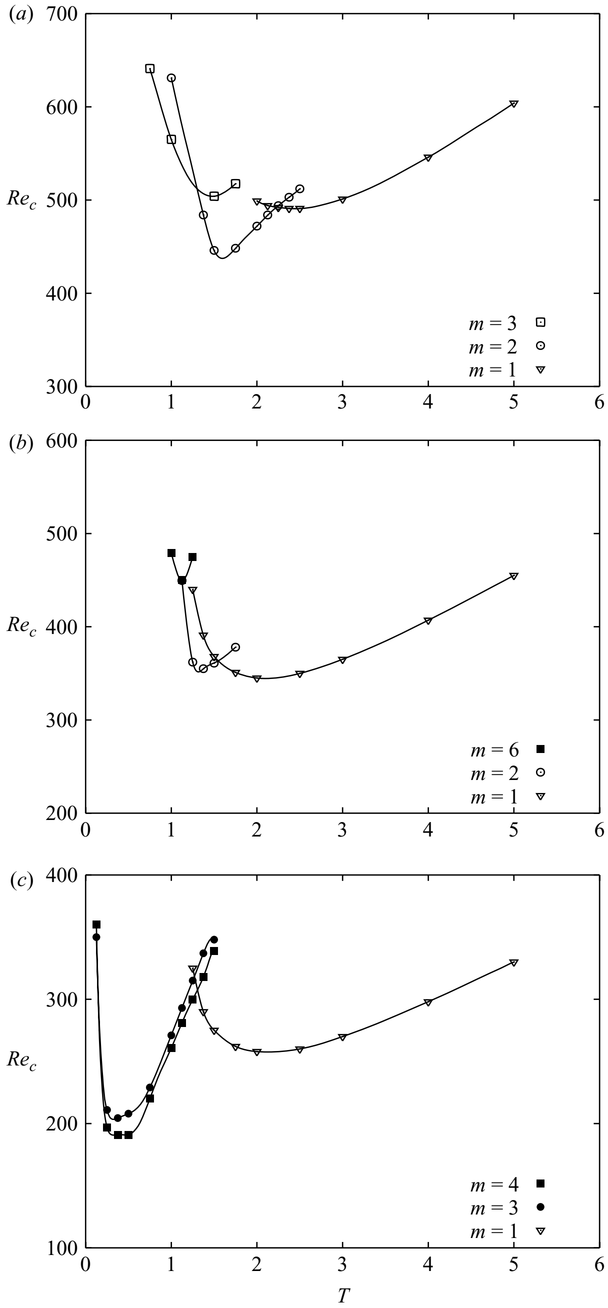

FIGURE 15. Critical Reynolds numbers of the leading azimuthal modes, of wavenumber m, for constant pulse amplitude $A = 0.75$ and three stenosis degrees (a) $b = 0.50$, (b) $b = 0.60$ and (c) $b = 0.75$, across the pulse period range. Hollow symbols indicate sub-harmonic period-doubling bifurcations.

obvious reason why this mode should be period-doubling, while the modes for $T \approx 1$ for $b = 0.60$ and 0.75 are synchronous with the base flow. In figure 18 there does appear to be a stronger interaction between the perturbation vorticity on successive

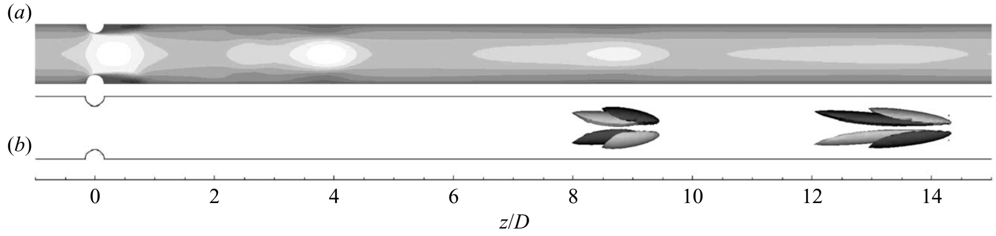

FIGURE 16. The base flow and the leading perturbation mode (period doubling), $m = 1$, for $b = 0.50$, $Re = 500$ and $T = 2.5$ ($\alpha = 17.7$) at phase $t = 0.0T$; (*a*) axial velocity contours of the unperturbed base flow; (*b*) equal-magnitude positive (light) and negative (dark) isosurfaces of axial vorticity of the perturbation mode.

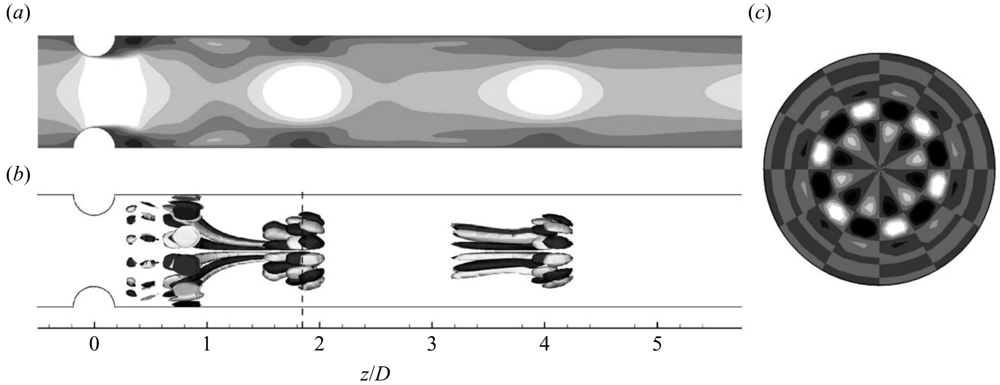

FIGURE 17. The base flow and the leading perturbation mode, $m = 6$, for $b = 0.60$, $Re = 480$ and $T = 1.0$ ($\alpha = 27.5$) at phase $t = 0.0T$; (*a*) axial velocity contours of the unperturbed base flow (white, positive; black, negative); (*b*) equal magnitude positive (light) and negative (dark) isosurfaces of axial vorticity of the perturbation mode; and (*c*) contours of axial vorticity of a cross-section of the perturbation at $z/D = 1.85$ or the dashed line in (*b*).

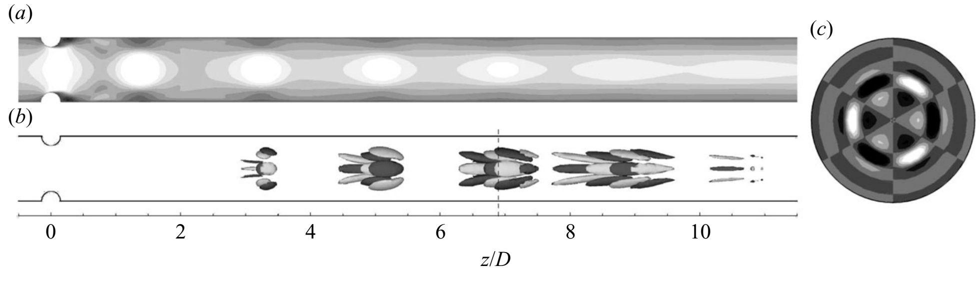

FIGURE 18. The base flow and plots of the period-doubling leading perturbation mode, $m = 3$, for $b = 0.50$, $Re = 575$ and $T = 1.0$ ($\alpha = 30.05$, at phase $t = 0.0T$; (*a*) axial velocity contours of the unperturbed base flow; (*b*) positive and negative isosurfaces of axial vorticity of the perturbation mode; and (*c*) positive and negative contours of axial vorticity of a cross-section of the perturbation at $z/D = 6.9$ or the dashed line in (*b*).

base flow vortex ringthan there is in the other two modes. Also, the mode appears to grow first around the flow in the centre of the tube and not close to the tube walls, as is the case for the leading mode for $b = 0.60$.

3.2.2. *Comparison to previous numerical work*

The $m = 1$ period-doubling mode is similar to that seen in the nearest comparable work in the literature, Sherwin & Blackburn (2005). However, for their stenotic geometry – consisting of a stenosis of $b = 0.75$ but with a longer length – they found a critical Reynolds number for pulse period $T = 2.5$ of $Re_c = 389$, with the perturbation vorticity reaching a maximum at $z/D \approx 20$. This is in contrast to the equivalent case for the present geometry (that of $b = 0.75$), where a critical Reynolds number of $Re_c = 260$ is found, with the downstream location of the maximum perturbation vorticity at $z/D \approx 15$. For shorter pulse periods, Blackburn & Sherwin (2007) also reported the presence of 'wavy modes' of wavenumber $m = 3$ and $m = 4$, which developed on the vortex ring, immediately downstream of the stenosis. Similar behaviour is observed for the current geometry of stenosis degree $b = 0.75$. In comparison to the work of Blackburn & Sherwin (2007), the optimum pulse periods for the $m = 1$ and the $m = 3$ and 4 wavy modes are much lower. In particular, for the $m = 4$ mode the optimum pulse period is $T \approx 0.4$, compared to $T = 0.875$ for the similar flow in Blackburn & Sherwin (2007). Also, the critical Reynolds number for the optimum pulse period is relatively much lower, as compared to the same value for the $m = 1$ period-doubling instability. The main difference between the two geometries is the much shorter contraction of the present geometry and the effect this has on the velocity profiles emerging from the contraction. This has a direct effect on the nature of the separating shear layer which forms downstream of the stenosis.

Most linear stability modes for pulsatile flow seen so far in the literature, and in the present work, begin their growth some distance downstream of the stenosis; the mode of figure 17 grows from the very beginning of the separating shear layer. As can be seen in figure 17(*b*), at $z/D \approx 0.85$, the perturbation is at its strongest on the walls of the tube, before aligning again with the tube centreline. It is possible that this behaviour is related to the phenomenon already observed in figure 11, where the vorticity topology in the near-wall vicinity for flows of pulse period, $T = 1.0$ differs from that of flows of longer pulse period. In figure 17(*a*), this behaviour can be seen as a small local maximum of axial velocity at $z/D \approx 1$, which may account for the altered stability behaviour seen for small pulse periods.

The question of how the linear stability analysis relates to the stability of the experimental results is discussed in the next section.

3.2.3. *Stability of the experimental flow*

While examining the experimental flows, it is useful to keep in mind the limits of instability for the steady flow through the same geometry, as presented in Griffith *et al.* (2008). For steady flow ($A = 0$), the limits for convective stability were found to be $Re_c \approx 900$ for $b = 0.50$, $Re_c \approx 400$ for $b = 0.75$ and $Re_c \approx 150$ for $b = 0.90$, for the experimental apparatus described in § 2.2. The Reynolds numbers for both steady and pulsatile flows are calculated in the same manner. However, the pulsatile flows also have an instantaneous Reynolds number, calculated using the time-dependent cross-sectional average velocity, $\overline{u}(t)$, rather than the temporal, cross-sectional average, $\overline{U}$. Therefore, the periodic Reynolds number is given by the formulation

$$Re_p(t) = \frac{D\overline{u}(t)}{\nu}. \tag{3.2}$$

Figure 19 shows coloured dye visualizations for two flows of stenosis degree $b = 0.50$. At left, the flow for $Re = 328$, $A = 0.75$ and $T = 3.92$, a configuration similar to that of figure 14, is presented. As before, the rolling up of the vortex ring can

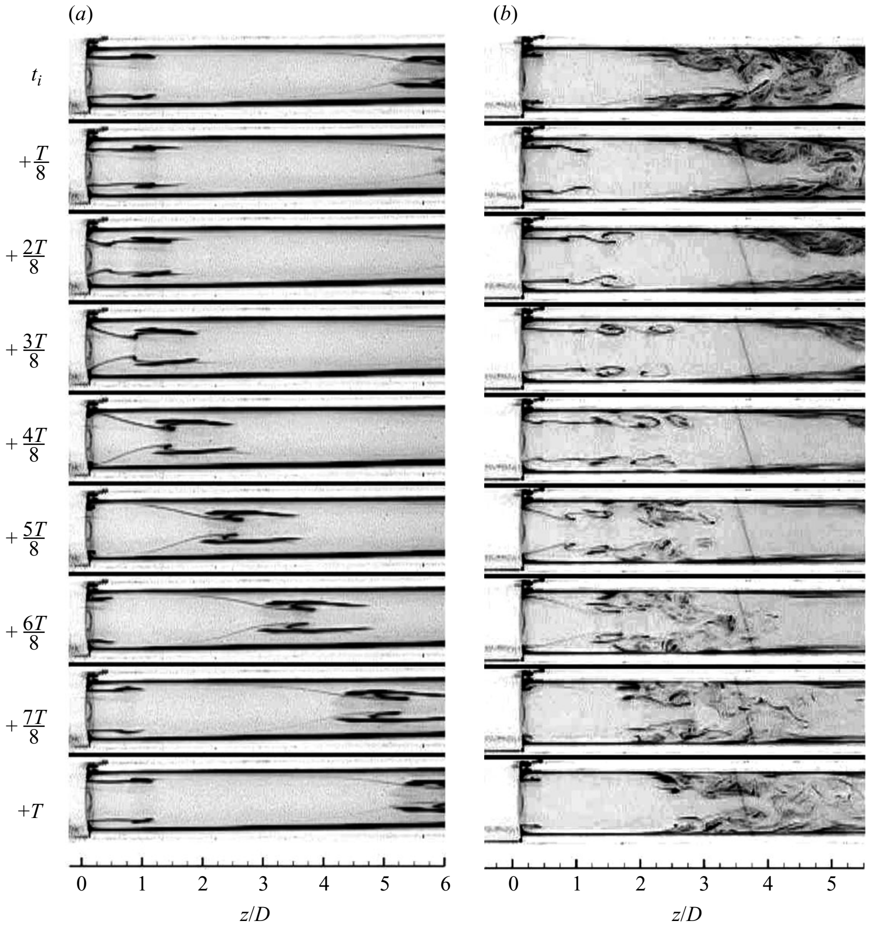

FIGURE 19. Coloured dye visualizations of the flow over one pulse period, for $b = 0.50$ and (*a*) $Re = 328$, $A = 0.75$ and $T = 3.92$ ($\alpha = 11.46$) and (*b*) $Re = 686$, $A = 0.5$ and $T = 4.31$ ($\alpha = 15.81$). (The phases between the two cases are not matched.)

be seen immediately downstream of the stenosis, followed by the stable progression downstream. From the earlier Floquet stability analysis, the flow is expected to be absolutely stable; indeed, experimentally, it is stable, with the same vortex structure of figure 19(*a*) repeating each pulsation period.

At right, in figure 19(*b*), are dye visualizations of the flow for a Reynolds number approximately twice that of the flow of figure 19(*a*), with a slightly greater pulse period; the pulse amplitude of $A = 0.50$ is also slightly lower. Upon considering the maximum values of the periodic Reynolds number for the two flow configurations, for the lower Reynolds number case $\hat{Re}_p = 574$, while for the higher Reynolds number case $\hat{Re}_p = 1029$ – the critical Reynolds number for convective instability for the steady flow of stenosis degree $b = 0.50$ is $Re_c \approx 900$. Hence, it is not surprising that strong unsteadiness is evident for the higher Reynolds number case.

In the first image shown, a large region of mixed dye can be seen around $z/D = 4$. In the subsequent images, this region convects rapidly downstream, indicating that the flow is in the systolic or accelerating portion of the pulse wave form. During this same period, the shear layer emanating from the stenosis can be seen developing

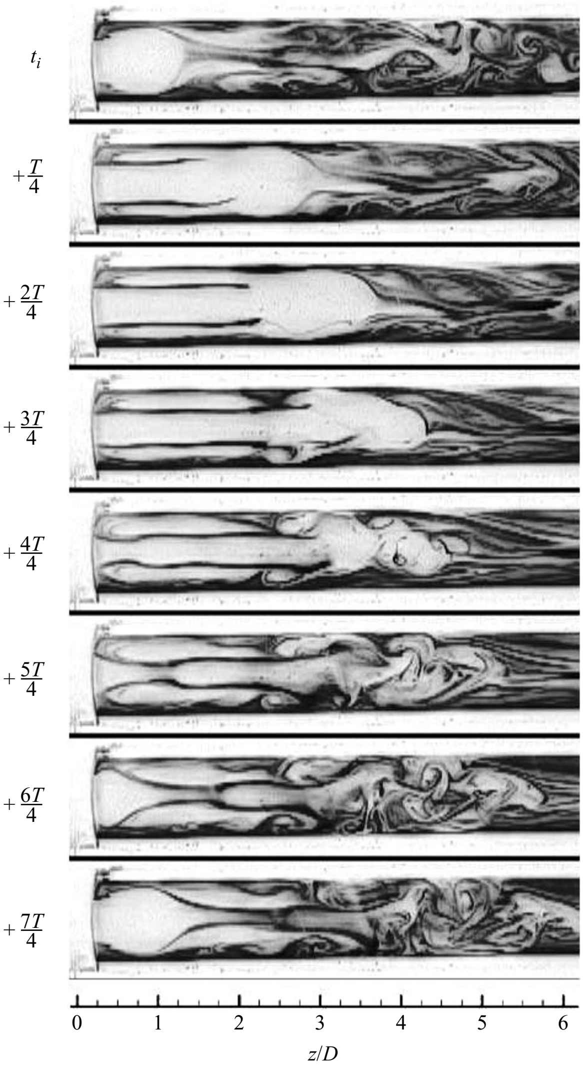

FIGURE 20. Coloured dye visualizations of the flow over one pulse period, for $b = 0.75$, $Re = 206$, $A = 0.75$ and $T = 2.43$ ($\alpha = 11.54$).

but not in a regular fashion. In the fourth of the series of images, at $t_i + (3T/8)$, a series of two distinct rolled-up vortices can be seen around $z/D = 2$. During the second half of the series of images, the diastole or deceleration period, the rolled-up shear layer vortices do not convect downstream but follow the pulse wave form, breaking down and causing a strongly mixed flow. The turbulent portion of flow then convects downstream with the mainstream pulse velocity. The instability appears to be strongly based on the convective shear layer roll-up. Not only does the instantaneous periodic Reynolds number exceed the threshold found for steady flow ($\approx$900), but the series of discrete shear layer vortices also is consistent with a Kelvin–Helmholtz-type instability.

Figure 20 presents dye visualizations over one pulse period of the flow of stenosis degree $b = 0.75$, Reynolds number $Re = 206$, pulse amplitude $A = 0.75$ and period $T = 2.43$. Floquet stability analysis of the numerical simulations predicts the flow to

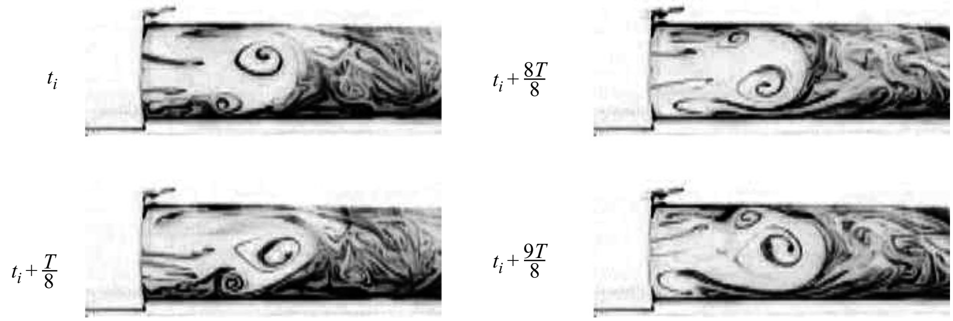

FIGURE 21. Coloured-dye visualizations highlighting the period-doubling instability, for $b = 0.75$, $Re = 132$, $A = 1.30$ and $T = 0.85$ ($\alpha = 15.8$). At left are shown two images at $t = t_i$ and $t = t_i + T/8$ and at right the flow one period later.

be absolutely stable (see figure 15*c*), while our maximum periodic Reynolds number is given by $\hat{Re}_p = 361$, which is on the threshold for convective instability in the steady flow in the present experimental apparatus (≈400). Some shear layer instability is therefore to be expected.

In the first image in figure 20, the flow at the end of the vortex formation phase is shown, with a large body of clear fluid from upstream rolling up into the main vortex ring, which subsequently convects downstream. For this configuration the flow is unstable but not as strongly as in the previous example; the shear layers emanating from the stenosis are clearly discernible over a large portion of the pulsation, with the greater part of the unsteadiness located further downstream. This will be further discussed later in the paper.

It is in experimental flows of stenosis degree $b = 0.75$ and pulsation amplitudes $A > 1$ that the clearest evidence of the period-doubling vortex-tilting instability reveals itself. Figure 21 presents several images of the flow for $Re = 132$, $A = 1.30$ and $T = 0.85$ ($\hat{Re}_p = 304$); to the left are images at $t = t_i$ and $t_i + T/8$, showing the vortex ring which forms immediately downstream of the stenosis tilting heavily from top to bottom, and to the right are shown the corresponding images exactly one period later. The vortex is tilting equally heavily in the opposite direction. Such configurations, with $b = 0.75$ and $A > 1$, were the only ones in which period doubling could be clearly detected.

In comparison with previous experimental work on single-harmonic pulsatile flows in stenotic geometries, the results presented here agree broadly with those in the literature (Ohja *et al.* 1989; Ahmed & Giddens 1983, 1984; Ahmed 1998). The flow configurations of Ohja *et al.* (1989) and Ahmed (1998) both consist of Womersley number $\alpha = 7.5$ and hence of longer pulse periods than most of the work presented in this paper. Nonetheless, at high enough Reynolds number, they both observed a stable jet region up to $z/D \approx 2.5$, with a transition and then breakdown of the flow at $z/D \approx 6$.

3.2.4. *Comparison to numerical stability analysis*

For stenosis degree $b = 0.50$ and $A = 0.75$, inspection of the flow for a range of Reynolds numbers revealed a boundary for $2 \leqslant T \leqslant 3$ of $Re_c \approx 350$ for stable vortex formation and convection downstream – as in figure 19(*a*). This critical Reynolds number is significantly smaller than the Floquet-predicted value for $T = 2.5$, of $Re_c = 491$ (see § 3.2.1); the mode predicted was of the period-doubling vortex-tilting type, although no evidence of this mode is detected for the experimental $b = 0.50$ flows. One possible reason for the difference between the critical Reynolds numbers is the convective nature of the instability in the experiments. A convective shear layer instability is not a mechanism detectable by our absolute linear Floquet stability analysis. Although the period-doubling phenomena were sought in the $b = 0.50$ flows, none was detected. In relation to the numerical stability analysis, the flows for stenosis degree $b = 0.75$ proved to be more interesting.

For the flow of figure 20 ($b = 0.75$, $Re = 206$, $A = 0.75$, $T = 2.43$), the flow breaks down approximately 4 to 5 diameters downstream of the stenosis. However, the shear layer roll-up of a Kelvin–Helmholtz-type instability is not as evident as in the previous example with $b = 0.50$. Indeed, any wave in the separating shear layer seems relatively gentle in comparison with the breakdown which occurs further downstream. Shear layer roll-up in the wake of the main vortex ring does not appear to be the main flow breakdown mechanism. In the downstream section of the first image in the series exists a substantial region of unsteadiness. It may be that the stability of the vortex ring formed during the following pulse period is affected by this and that the unsteadiness is self-sustaining from one period to the next rather than fed from shear layer vortices formed slightly upstream.

The clearest evidence of period doubling was seen in flows of pulse amplitude $A > 1$ and $b = 0.75$ (e.g. figure 21). Special note needs to be made here of the conditions under which this particular behaviour is observed. Firstly, Floquet stability analysis of a numerical simulation of this flow predicts it would be stable. Secondly, the position and growth of the instability is not consistent with the period-doubling vortex-tilting mode predicted earlier in this paper or with the mode predicted in Sherwin & Blackburn (2005) for a similar geometry of $b = 0.75$. Numerically, the mode growth occurs far downstream. Direct numerical simulations of the three-dimensional flow in Sherwin & Blackburn (2005) showed the instability slowly progresses upstream, with a flow breakdown settling 4–5 diameters downstream of the stenosis. However, this ‘settling in’ of the unsteadiness occurred over very long time scales. In the case of figure 21, the instability is apparent directly downstream of the stenosis and appears within two periods of the pulsation beginning – there is no slow upstream progression. Therefore, the initial vortex tilting may be dependent on the pulsation initialization or simply grow quickly.

In every observed instance of the phenomenon, the instability acted in the vertical plane. The instability aligns with a preferred direction; it is probable that in the experiment the choice of plane is influenced by the direction of the gravitational force. As mentioned in § 2.2, temperature differences between the fluid in the tube and the fluid in the visualization box can have an effect on flows. The heating or cooling of fluid through the tube walls can lead to convection in the tube, causing asymmetries in the flow. This source of error is minimized as far as possible; yet it still remains, if only at a low level. Even at this scale, the bias direction may be enough to influence the direction of the vortex tilting, once the flow has become critical and the instability appears. A similar phenomenon – where the orientation of an asymmetric instability on an axisymmetric base flow fixes at a certain angle on a given experimental rig – has been observed previously in work on the wake flows of spheres (Leweke *et al.* 1999).

A possible clue to the presence of the phenomenon can be found in Blackburn & Sherwin (2007), where the interaction between convective shear layer instability and the absolute period-doubling vortex-tilting instability was investigated. Floquet stability analysis was performed on a base pulsatile flow already perturbed by a

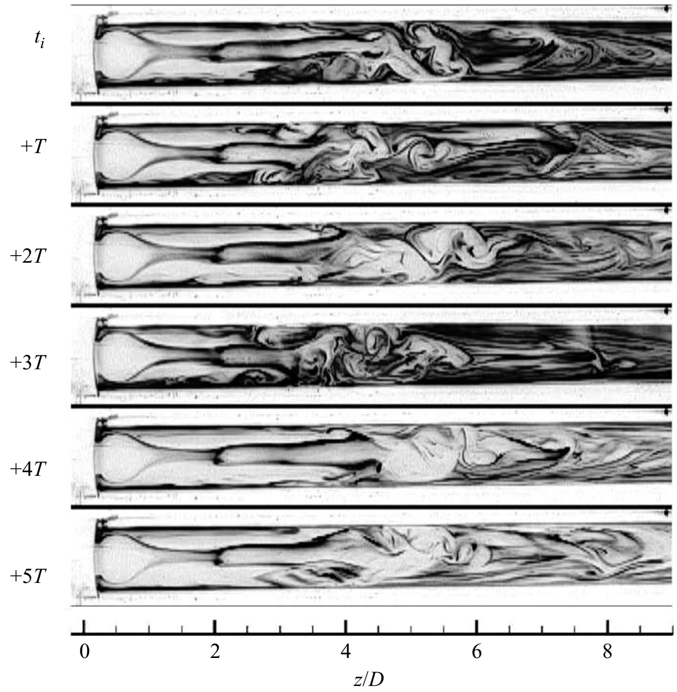

FIGURE 22. Coloured dye visualizations of the flow over six pulse periods, with each image at the same phase, for $b = 0.75$, $Re = 206$, $A = 0.75$ and $T = 2.43$ ($\alpha = 11.54$).

low-amplitude, high-frequency forcing. At large pulse periods, they found Floquet multipliers much greater than those found performing the stability analysis on unperturbed flows. Furthermore, the peak strengths of the perturbation modes moved far upstream. Direct numerical simulation of the perturbed flow, at $Re = 600$, $A = 0.75$ and $T = 10$, revealed a response strong enough that the period-doubling nature of the instability was no longer detectable. They did not calculate critical stability boundaries for these perturbed flows.

Therefore, we return to the flow of figure 20 ($b = 0.75$, $Re = 206$, $A = 0.75$, $T = 2.43$), in order to verify if any evidence of period doubling can be detected, even though our Floquet analysis of the numerical simulation predicts the flow to be absolutely stable. Figure 22 replots the flow, this time at the same phase over six consecutive periods. The flow is unsteady, but there are indications of tilting in the flow breakdown which occurs at $4 < z/D < 6$. Perhaps the clearest indication is in the first and third images, where the flow breakdown appears to have a similar upward-tilting bias ($z/D \approx 5$). The indications of period doubling in the flow are tenuous; however, it is not expected that there should necessarily be a strong indication in the asymptotic flow.

4. Conclusions

This paper has presented investigations of various aspects of pulsatile flow through axisymmetric stenotic geometries. In particular, it has focused on the wake behaviour and stability of the flow for different stenosis degrees. The dye visualizations constitute a technique which has so far not been used extensively in experimental work on the subject.

The velocity of the vortex ring which forms downstream of the stenosis each period of a pulsatile flow has been analysed. Driven by the circulation generated through the stenosis, the vortex rings travel downstream, faster at higher stenosis degrees than at lower ones. For a pulse period $T = 2.5$, it was found that the normalized vortex ring velocity, V_v, increases for lower stenosis degrees, for $b \gtrsim 0.4$. This is possibly due to a higher proportion of the generated circulation collecting in the trail of the vortex or due to the higher axial velocities of the vortex ring for higher stenosis degrees, which may induce a stronger viscous drag via the tube walls.

The variation of the wall shear stress for several flow configurations was described, with a higher maximum wall shear stress observed for cases at lower pulse periods and higher stenosis degrees. It was found that the time-averaged wall shear stress distribution for pulsatile flow matches closely with that of the corresponding steady flow. It is only for lower pulse periods of $T \approx 1$ that the two distributions begin to significantly diverge. For the cases considered, for pulse periods greater than one, flows exhibit low average wall shear stresses (where the average wall shear stress changes sign) in the range $4 \lesssim z/D \lesssim 6$.

Across the three stenosis degrees tested, Floquet stability analysis with a constant pulse amplitude $A = 0.75$ shows a period-doubling vortex-tilting perturbation mode of wavenumber $m = 1$ dominating for pulse periods $T > 1.2$ for $b = 0.75$ and $T > 2.2$ for $b = 0.50$, while for lower pulse periods, higher wavenumber modes dominate. For the higher Womersley number (lower pulse period) range, the vortex-tilting mechanism is overtaken by higher wavenumber modes, including $m = 3$ and $m = 4$ bifurcations for $b = 0.75$. In the cases of $b = 0.50$ and 0.60, the stability behaviour was similar to that observed in Griffith *et al.* (2008) for steady flow, with the $m = 2$ mode overtaking the $m = 1$ sub-harmonic bifurcation. For still higher Womersley numbers, an $m = 6$ real bifurcation was observed for $b = 0.60$ and an $m = 3$ sub-harmonic bifurcation for $b = 0.50$.

The initial growth of the $m = 1$ period-doubling mechanism begins far downstream of the stenosis. Its axial location of maximum strength varies with the stenosis degree but appears to be dependent on the different vortex ring velocities. The only firm evidence of any period-doubling instability in the experimental flow occurred for a stenosis degree of $b = 0.75$ but only for pulse amplitudes of $A > 1$. For these flows, vortex rings tilt in opposite radial directions each pulse period. However, this particular form of tilting only occurs on the vertical plane and is generated as soon as the pulsation is begun rather than progressing slowly upstream from a downstream location. Instabilities for flow configurations just below the critical boundary predicted by the numerical analysis did not exhibit obvious evidence of period doubling, but their nature is at least consistent with the action of a linear instability mode.

For the stenosis degree $b = 0.50$, convective instability seems to be the major cause of instability. A number of unstable flows were observed where the formation of discrete vortices in the separating shear layer could be discerned every pulse period; this bears the hallmark of a Kelvin–Helmholtz-type instability. Evidence could not be found of the linear instability modes predicted by the Floquet stability analysis for $b = 0.50$. Using the concept of an instantaneous Reynolds number $Re_p(t)$, it was found that the stability of the flow depended roughly on the maximum value of this periodic Reynolds number remaining below the critical Reynolds number for convective instability in the steady flow.

The authors gratefully acknowledge financial support from the Australian Research Council (ARC Discovery Project Grant DP0555897 and ARC Linkage International

Grant LX0668992) and the Embassy of France in Australia. The first author would also like to acknowledge the assistance of a Postgraduate Publication Award from the Monash Research Graduate School.

REFERENCES

AHMED, S. A. 1998 An experimental investigation of pulsatile flow through a smooth constriction. *Exp. Therm. Fluid Sci.* **17**, 309–318.

AHMED, S. A. & GIDDENS, D. P. 1983 Flow disturbance measurements through a constricted tube at moderate Reynolds numbers. *J. Biomech.* **16**, 955–963.

AHMED, S. A. & GIDDENS, D. P. 1984 Pulsatile poststenotic flow studies with laser doppler anemometry. *J. Biomech.* **17**, 695–705.

BERGER, S. A. & JOU, L-D. 2000 Flows in stenotic vessels. *Annu. Rev. Fluid Mech.* **32**, 347–382.

BLACKBURN, H. M. & SHERWIN, S. J. 2007 Instability modes and transition of pulsatile stenotic flow: pulse-period dependence. *J. Fluid Mech.* **573**, 57–88.

CASSANOVA, R. A. & GIDDENS, D. P. 1978 Disorder distal to modified stenoses in steady and pulsatile flow. *J. Biomech.* **11**, 441–453.

DEPLANO, V. & SIOUFFI, M. 1999 Experimental and numerical study of pulsatile flows through stenosis: wall shear stress analysis. *J. Biomech.* **32**, 1081–1090.

GHARIB, M, RAMBOD, E. & SHARIFF, K. 1998 A universal time scale for vortex ring formation. *J. Fluid Mech.* **360**, 121–140.

GRIFFITH, M. D. 2007 The stability and behaviour of flows in stenotic geometries. PhD thesis, Department of Mechanical Engineering, Monash University, Melbourne, Australia.

GRIFFITH, M. D., LEWEKE, T., THOMPSON, M. C. & HOURIGAN, K. 2008 Steady inlet flow in stenotic geometries: convective and absolute instabilities. *J. Fluid Mech.* **616**, 111–133.

GRIFFITH, M. D., THOMPSON, M. C., LEWEKE, T., HOURIGAN, K. & ANDERSON, W. P. 2007 Wake behaviour and instability of flow through a partially blocked channel. *J. Fluid Mech.* **582**, 319–340.

KHALIFA, A. M. A. & GIDDENS, D. P. 1978 Analysis of disorder in pulsatile flows with application to poststenotic blood velocity measurement in dogs. *J. Biomech.* **11**, 129–141.

KHALIFA, A. M. A. & GIDDENS, D. P. 1981 Characterization and evolution of poststenotic disturbances. *J. Biomech.* **14**, 279–296.

KU, D. N. 1997 Blood flow in arteries. *Annu. Rev. Fluid Mech.* **29**, 399–434.

LEWEKE, T., PROVANSAL, M., ORMIERES, D. & LEBESCOND, R. 1999 Vortex dynamics in the wake of a sphere. *Phys. Fluids* **11**, S12.

LIEBER, B. B. & GIDDENS, D. P. 1990 Post-stenotic core flow behaviour in pulsatile flow and its effects in wall shear stress. *J. Biomech.* **23**, 597–605.

LIU, H. & YAMAGUCHI, T. 2001 Waveform dependence of pulsatile flow in a stenosed channel. *J. Biomech. Engng* **123**, 88–96.

LOUDON, C. & TORDESILLAS, A. 1998 The use of the dimensionless Womersley number to characterize the unsteady nature of internal flows. *J. Theor. Biol.* **191**, 63–78.

MALLINGER, F. & DRIKAKIS, D. 2002 Instability in three-dimensional, unsteady, stenotic flows. *Intl J. Heat Fluid Flow* **23**, 657–663.

MEUNIER, P. & LEWEKE, T. 2003 Analysis and treatment of errors due to high velocity gradients in particle image velocimetry. *Exp. Fluids* **35**, 408–421.

OHJA, M., COBBOLD, R. S. C., JOHNSTON, K. W. & HUMMEL, R. L. 1989 Pulsatile flow through constricted tubes: an experimental investigation using photochromic tracer methods. *J. Fluid Mech.* **203**, 173–197.

SHEARD, G. S., THOMPSON, M. C. & HOURIGAN, K. 2003 From spheres to circular cylinders: the stability and flow structures of bluff ring wakes. *J. Fluid Mech.* **492**, 147–180.

SHERWIN, S. J. & BLACKBURN, H. M. 2005 Three-dimensional instabilities of steady and pulsatile axisymmetric stenotic flows. *J. Fluid Mech.* **533**, 297–327.

STROUD, J. S., BERGER, S. A. & SALONER, D. 2000 Influence of stenosis morphology in flow through severely stenotic vessels: implications for plaque rupture. *J. Biomech.* **33**, 443–455.

THOMPSON, M. C., HOURIGAN, K. & SHERIDAN, J. 1996 Three-dimensional instabilities in the wake of a circular cylinder. *Exp. Therm. Fluid Sci.* **12**, 190–196.

Thompson, M. C., Leweke, T. & Provansal, M. 2001 Kinematics and dynamics of sphere wake transition. *J. Fluids Struct.* **15**, 575–585.

Tu, C., Deville, M., Dheur, L. & Vanderschuren, L. 1992 Finite element simulation of pulsatile flow through arterial stenosis. *J. Biomech.* **25**, 1141–1152.

Varghese, S. S. & Frankel, S. H. 2003 Numerical modelling of pulsatile turbulent flow in stenotic vessels. *J. Biomech. Engng* **125**, 445–460.

Varghese, S. S., Frankel, S. H. & Fischer, P. F. 2007 Direct numerical simulation of stenotic flows. Part 2. Pulsatile flow. *J. Fluid Mech.* **582**, 281–318.

Widnall, S. E., Bliss, D. B. & Tsai, C.-Y 1974 The instability of short waves on a vortex ring. *J. Fluid Mech.* **66**, 35–47.

Womersley, J. R. 1955 Method for the calculation of velocity, rate of flow and viscous drag in arteries when their pressure gradient is known. *J. Physiol.* **127**, 553–563.

Wootton, D. M. & Ku, D. N. 1999 Fluid mechanics of vascular systems, diseases, and thrombosis. *Annu. Rev. Biomed. Engng* **1**, 299–329.